

# Drop dynamics in an oscillating extensional flow at finite Reynolds numbers

Xiaoyi Li and Kausik Sarkar

*Department of Mechanical Engineering, University of Delaware, Newark, Delaware 19716*

(Received 16 June 2004; accepted 5 November 2004; published online 13 January 2005)

A viscous drop deforming in a planar oscillating extensional flow is numerically simulated using a front-tracking finite-difference method. The effects of periodic forcing and interfacial tension are studied at low but finite inertia. The oscillation leads to decreased deformation and bounded drop shapes for conditions for which steady extension results in drop breakup. The drop displays a resonance phenomenon where the deformation reaches a maximum when the forcing frequency matches the natural frequency of the drop. The large deformation at resonance indicates a possible mechanism for size selective breakup by flows with appropriate fluctuation frequency. The detail structure of the flow at different time instants within a period for various values of interfacial tension and frequency is investigated. The drop dynamics shows a complex phase relation with the forcing flow. Competition between the inertia-induced dynamic pressure and the viscous stresses leads to both positive and negative values of the phase and a complex variation with interfacial tension and forcing frequency. A second-order ordinary differential equation model with appropriate representation of the pressure and viscous forces is developed that qualitatively explains the phase behaviors. For the highest inertia case considered in this paper ( $Re=10.0$ ), the drop dynamics becomes aperiodic at resonance marked by a strong subharmonic component in the frequency spectrum. © 2005 American Institute of Physics. [DOI: 10.1063/1.1844471]

## I. INTRODUCTION

Emulsions of immiscible drops with complex rheological behavior appear in a number of industrial applications. The shape, orientation, and size distribution of interacting drops along with their material properties govern the non-Newtonian stresses in these flows.<sup>1,2</sup> Recognizing the critical role played by the dynamics of a single drop, researchers have extensively studied it since the pioneering work of Taylor on a drop deforming in linear flows.<sup>3,4</sup> For the most part, previous research has been restricted to *inertialless steady Stokes flow* using various asymptotic methods<sup>5-9</sup> and boundary element simulation.<sup>10</sup> The latter allows simulation of arbitrary deformation as well as strongly interacting drops in a concentrated emulsion.<sup>11,12</sup> On the experimental side, Grace<sup>13</sup> reported several criteria for breakup with varying viscosity ratios in pure shear and extensional flows. The effects of flow type were systematically investigated by Bentley and Leal<sup>14</sup> using a computer-controlled four-roll mill. Experiments were performed on drop behaviors in shear reversal<sup>15</sup> and drop relaxation after step shear.<sup>16</sup> With a view to predicting rheology of emulsion, recently a number of new analytical ellipsoidal droplet models<sup>17-19</sup> have been developed with various degrees of success in matching experimental observations. Although many applications involve significantly high Reynolds numbers, much less attention has been paid to the effects of inertia on drop deformation and breakup. Leal and co-workers<sup>20-22</sup> conducted a series of studies of inertial effects on drop deformation in uniaxial extensional flows. Inertia increases deformation. It gives rise to a dynamic pressure that dominates the viscous stress to produce a barrel-like drop shape. The deformation displays a

complex dependence on viscosity and density ratios.<sup>20</sup> At large density ratio, increased drop viscosity leads to higher damping, thus decreased deformation. Renardy *et al.*<sup>23,24</sup> numerically simulated breakup of an isolated drop in a shear flow at finite Reynolds number, and found that the critical Reynolds number for breakup scales with inverse capillary number. Along with inertia, oscillation and fluctuation remain the other important yet much less investigated aspects in the deformation research. Turbulent flow of emulsion offers a case with such oscillations due to eddies of all possible length scales and frequencies interacting with drops. On the other hand, over the years oscillatory shear has become a standard rheometer for testing the rheological properties of emulsions.<sup>25,26</sup> Recently, the deformation and breakup of drops in slow oscillatory shear have been experimentally investigated<sup>27,25</sup> with results matched by both direct numerical simulation<sup>27</sup> and linear viscoelastic theory.<sup>28</sup>

Recently, Sarkar and Schowalter<sup>29</sup> have numerically investigated the deformation of a two-dimensional drop in the flow field of a vortex and related extensional flows with rotating axes of extension. They observed unusual phenomena due to resonance such as increased drop deformation for increasing surface tension in such time-periodic straining flows. The drop acts as a damped mass-spring system, where surface tension and viscosity play the roles of the spring and damping elements, and the finite inertia, that of the mass. As the interfacial tension is varied the natural frequency of the system changes, and when it matches the forcing frequency, the deformation attains a maximum. Subsequent small amplitude perturbative analysis<sup>30</sup> using unsteady Stokes solution of the system further elucidated the resonant drop dy-

namics. Resonance may provide an alternative mechanism for efficient energy transfer from flow to the drop, and result in its breakup at low strain amplitude but appropriate frequency.<sup>31</sup> In an experimental investigation of a turbulent flow of bubbly liquid, Risso and Fabre<sup>32</sup> observed bubble breakup controlled by a similar resonance-like mechanism. It should further be stressed that even for Stokes flow without inertia, the history of the unsteady flow is critical for the determination of the dynamic behavior of drops. For example, at subcritical flow conditions where the drop does not breakup according to steady analysis, an abrupt change in strain rate or flow type may induce breakup.<sup>33,34</sup>

Here, we investigate the deformation of a three-dimensional drop in an oscillating extensional flow at finite inertia. The flow can be realized using a four-roll mill.<sup>3,14</sup> We adopt a three-dimensional version of the front-tracking finite-difference<sup>35,36</sup> code that we used for our previous investigations.<sup>29,37</sup> In the following, the mathematical formulation and its numerical implementation are briefly described. We developed a second-order ordinary differential equation (ODE) model that adequately captures the underlying physics and explains the numerical observations. A systematic investigation is conducted by varying Reynolds number, interfacial tension, and flow frequency. The resulting drop dynamics and the modified flow field are described in detail, and their relations discussed.

## II. OSCILLATING EXTENSIONAL FLOW

We assume a planar oscillating extensional flow:

$$\begin{pmatrix} u \\ v \\ w \end{pmatrix} = \dot{\epsilon}_0 \cos(\omega t) \begin{pmatrix} 0 & 1 & 0 \\ 1 & 0 & 0 \\ 0 & 0 & 0 \end{pmatrix} \begin{pmatrix} x \\ y \\ z \end{pmatrix}. \quad (1)$$

Here,  $\dot{\epsilon}_0$  is the maximum strain rate. The principle axis of extension oscillates with the angular frequency  $\omega$ . Note that the flow is free of vorticity. However, presence of the drop results in vorticity generation, as will be seen below. Also note that the drop induces a nonzero  $w$  velocity component, although the forcing flow is purely planar.

## III. MATHEMATICAL FORMULATION

With a drop of Newtonian liquid suspended in another Newtonian liquid, the flow is governed by the (Navier-Stokes) equation:<sup>29,35,36</sup>

$$\frac{\partial(\rho\vec{u})}{\partial t} + \nabla \cdot (\rho\vec{u}\vec{u}) = -\nabla p + \nabla \cdot [\mu \nabla \vec{u} + (\mu \nabla \vec{u})^T] - \int_{\partial B} d\vec{x}_B \kappa \vec{n} \Gamma \delta(\vec{x} - \vec{x}_B), \quad (2)$$

where  $p$  is the pressure,  $\rho$  the local density of the fluid, and  $\mu$  the local viscosity. The superscript  $T$  represents transpose. The velocity  $\vec{u}$  is continuous in the entire domain  $\Omega$ , which consists of the continuous phase  $\Omega_c$  and the suspended drop  $\Omega_d$  as shown in Fig. 1(a).  $\partial B$  is the drop-fluid interface consisting of points  $\vec{x}_B$ ,  $\Gamma$  is the constant interfacial tension,  $\kappa$  the local curvature,  $\vec{n}$  the outward normal to the interface,

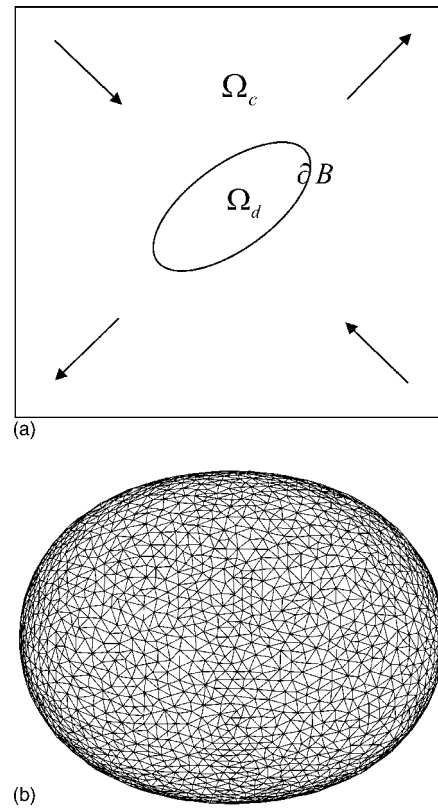


FIG. 1. (a) Schematic of the domain of calculation. (b) Discretized drop interface by triangular elements.

and  $\delta(\vec{x} - \vec{x}_B)$  is the three-dimensional Dirac delta function. The interfacial tension, which produces a jump in the normal stress across the interface, is represented as a singular body force<sup>29,35,36</sup> anticipating its numerical implementation. The variation of interfacial tension  $\Gamma$  due to a nonuniform distribution of surfactant is not considered. The fluid is incompressible in both phases:

$$\nabla \cdot \vec{u} = 0. \quad (3)$$

The interface follows the fluid. The kinematic condition for the interface is

$$\frac{d\vec{x}_B}{dt} = \vec{u}(\vec{x}_B). \quad (4)$$

The velocity on the interface  $\vec{x}_B$  is related to the field velocity

$$\vec{u}(\vec{x}_B) = \int_{\Omega} d\vec{x} \delta(\vec{x} - \vec{x}_B) \vec{u}(\vec{x}). \quad (5)$$

## IV. NUMERICAL IMPLEMENTATION

The above formulation leaves us with a system of partial differential equations with spatially varying coefficients. Conventionally, the Navier-Stokes equation needs to be solved for each phase, matching boundary conditions at the interface. Front-tracking method<sup>35,36</sup> treats the entire flow system as a single phase with a sharp variation of properties

in a finite-thickness region across the interface. A smooth representation of the  $\delta$  functions in (2) and (5) is used for the numerical implementation:

$$D(\vec{x} - \vec{x}_B) = D^1(x - x_B)D^1(y - y_B)D^1(z - z_B),$$

$$D^1(x - x_B) = \frac{1}{4\Delta x} \left( 1 + \cos \frac{\pi}{2\Delta x} (x - x_B) \right), \quad (6)$$

$$|x - x_B| \leq 2\Delta x.$$

$\Delta x$  is grid spacing for the discretization. The Navier-Stokes equation is solved in a discretized domain containing both the drop  $\Omega_d$  and the continuous phase  $\Omega_c$ . The drop interface (front) is represented by a separate mesh composed of triangular elements as shown in Fig. 1(b). To prevent the elements from being excessively distorted, an adaptive regriding scheme is implemented for the front. The motion of the element vertices determines the shape of the evolving interface.

The velocity and pressure are described on a staggered grid. The Navier-Stokes equation is solved by operator splitting projection finite-difference method. The method solves the equations in two steps. The first step is to find an intermediate velocity  $\vec{u}^*$  by

$$\frac{\rho^{n+1} \vec{u}^* - (\rho \vec{u})^n}{\Delta t} = -\nabla \cdot (\rho \vec{u} \vec{u})^n + \vec{F}^n + \nabla \cdot \vec{\tau}^n, \quad (7)$$

where  $\vec{\tau}^n$  is the viscous stress.  $\vec{F}^n$  is the body force, here arising solely from interfacial tension. The spatial derivatives are approximated by central differences in their conservative form. The final velocity at next time step  $\vec{u}^{n+1}$  is obtained by

$$\frac{\vec{u}^{n+1} - \vec{u}^*}{\Delta t} = -\frac{1}{\rho^{n+1}} \nabla p^{n+1}, \quad (8)$$

where the pressure  $p^{n+1}$  is calculated by requiring  $\vec{u}^{n+1}$  to be divergence-free [Eq. (3)]. Thus a Poisson's equation for pressure needs to be solved,

$$\nabla \cdot \left( \frac{1}{\rho^{n+1}} \nabla p^{n+1} \right) = \frac{1}{\Delta t} \nabla \cdot \vec{u}^*. \quad (9)$$

We use a multigrid method for solving the pressure Poisson's equation.

As indicated in previous study,<sup>29</sup> a fully explicit scheme for calculating the stress  $\nabla \cdot \vec{\tau}^n$  suffers from restrictions on time steps  $\Delta t < 0.125(\Delta x)^2 \rho / \mu$ , especially at low Reynolds numbers. To overcome this restriction, we treat some of the diffusive terms implicitly in alternate spatial directions (ADI). The viscous term in Eq. (7) can be expressed as

$$\nabla \cdot \vec{\tau}^n = D_{xy} + D_{yz} + D_{zx} + D_{zz} + D_{yy} + D_{xx}, \quad (10)$$

where  $D_{xy}$ ,  $D_{yz}$ ,  $D_{zx}$  are the mixed derivatives, and are computed by an explicit scheme.  $D_{zz}$ ,  $D_{yy}$ ,  $D_{xx}$  are the double derivatives to be treated implicitly. With ADI, the Eq. (7) is further split into four steps:

$$\frac{\rho^{n+1} \vec{u}^{* * * *} - (\rho \vec{u})^n}{\Delta t} = -\nabla \cdot (\rho \vec{u} \vec{u})^n + \vec{F}^n + D_{xy}(\vec{u}^n) + D_{yz}(\vec{u}^n) + D_{zx}(\vec{u}^n), \quad (11)$$

$$\rho^{n+1} \frac{\vec{u}^{* * * *} - \vec{u}^{* * * *}}{\Delta t} = D_{zz}(\vec{u}^{* * * *}), \quad (12)$$

$$\rho^{n+1} \frac{\vec{u}^{* * * *} - \vec{u}^{* * * *}}{\Delta t} = D_{yy}(\vec{u}^{* * * *}), \quad (13)$$

$$\rho^{n+1} \frac{\vec{u}^{* * * *} - \vec{u}^{* * * *}}{\Delta t} = D_{xx}(\vec{u}^{* * * *}). \quad (14)$$

Each implicit equation (12)–(14) gives rise to a tridiagonal system that is directly solved without iteration. The convergence of the scheme is ensured by prescribing for the intermediate velocities at the boundary  $\partial\Omega$  (Ref. 29) as

$$\vec{u}^* = \vec{u}^{* * * *} = \vec{u}^{* * * *} = \vec{u}^{* * * *} = \vec{u}^{n+1}. \quad (15)$$

The ADI scheme reduces the time step by one order of magnitude. We also adhere to other criteria  $\Delta t < 2.0\mu / (\rho U_{\max}^2)$  and  $\Delta t < \Delta x / U_{\max}$  at high Reynolds numbers to ensure the overall convergence of our simulations.

## V. NONDIMENSIONAL PARAMETERS

The mathematical problem can be nondimensionalized using the undeformed drop radius  $R$  and the inverse extensional rate  $\dot{\epsilon}_0^{-1}$  as the length and the time scales, respectively. In this paper, in the interest of brevity, we have restricted ourselves to density and viscosity ratios to the value of unity. Note that the present numerical scheme can handle different density and viscosity inside the drop. Three nondimensional parameters define the problem. They are Reynolds number  $Re = \rho \dot{\epsilon}_0 R^2 / \mu$ , inverse capillary number  $k = Ca^{-1} = \Gamma / (\dot{\epsilon}_0 \mu R)$ , and nondimensional frequency (Strouhal number)  $St = \omega / \dot{\epsilon}_0$ . Typical values for a drop of alcohol insoluble in water are  $\mu = 0.018 \text{ g cm}^{-1} \text{ s}^{-1}$ ,  $\rho = 0.82 \text{ g cm}^{-3}$ , and  $\Gamma = 1-10 \text{ dynes cm}^{-1}$  (Davies and Rideal<sup>38</sup> p. 17). For such a drop of radius,  $R = 1 \text{ cm}$ , suspended in water ( $\mu = 0.01 \text{ g cm}^{-1} \text{ s}^{-1}$ ,  $\rho = 1.0 \text{ g cm}^{-3}$ , and  $\dot{\epsilon}_0 = 0.1 \text{ s}^{-1}$ ), one obtains  $Re = 10$  and  $k = 1000-10000$ .

## VI. A SIMPLE SECOND-ORDER ODE MODEL

Although the flow is governed by the Navier-Stokes equation, the underlying physics of drop deformation can be described by a simple ODE model as has been demonstrated by Sarkar and Schowalter.<sup>29,37</sup> A drop subjected to a linear extensional flow can be modeled as a damped mass-spring system with mass  $\hat{\rho} \hat{R}^3$ , damping  $\hat{\mu}$  (viscosity), and spring  $\hat{\Gamma}$  (interfacial tension).  $\hat{R}$  is the drop radius. The hat is used to differentiate the model variables from their real counterparts. Forced by the imposed flow  $G_0 g(t)$  ( $G_0$  is the magnitude), deformation of the drop is modeled by a second-order ODE representing a harmonic oscillator:

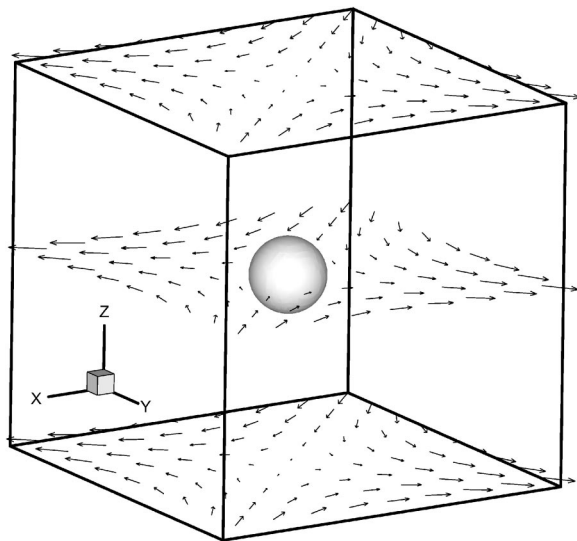


FIG. 2. The drop in the computational domain with an oscillating extensional flow imposed at the boundary.

$$\hat{\rho}\hat{R}^3\ddot{X} + \hat{\mu}\hat{R}\dot{X} + \hat{\Gamma}X = \hat{\mu}\hat{R}G_0g(t) + \hat{\rho}\hat{R}^3G_0\dot{g}(t). \quad (16)$$

The initial condition is

$$\dot{X}(0) = G_0g(0), \quad X(0) = 0. \quad (17)$$

The forcing terms in the right-hand side of Eq. (16) are chosen to mimic the effects of the forcing flow. The first forcing term corresponds to the viscous stress and the second term represents the dynamic pressure. From the momentum equation (2),  $\rho\partial u/\partial t \sim \nabla p$ , one can see that a time-dependent velocity  $G_0g(t)$  gives rise to such a pressure. As we will see, the pressure gradient plays a crucial role in the drop dynamics, and the inclusion of the second term in the forcing is critical for accurate description of the underlying physics. An oscillating flow is specified by  $g(t) = \exp(i\omega t)$ .

The model is nondimensionalized using the length scale  $\hat{R}$  and time scale  $\hat{R}/G_0$ :

$$\hat{Re} \ddot{X} + \hat{X} + \hat{k}X = g(t) + \hat{Re} \dot{g}(t), \quad (18)$$

$$\dot{X}(0) = g(0), \quad X(0) = 0, \quad g(t) = \exp(it \hat{St}), \quad (19)$$

where the nondimensional numbers are  $\hat{Re} = \hat{\rho}\hat{R}G_0/\hat{\mu}$ ,  $\hat{k} = \hat{\Gamma}/(\hat{\mu}G_0)$ ,  $\hat{St} = \omega\hat{R}/G_0$ , and  $t' = tG_0/\hat{R}$ . The solution of this ODE is

$$X = \frac{1 + i \hat{Re} \hat{St}}{\hat{k} - \hat{Re} \hat{St}^2 + i \hat{St}} \exp(it \hat{St}), \quad (20)$$

with a magnitude

$$|X| = \sqrt{\frac{1 + \hat{St}^2 \hat{Re}^2}{[\hat{k} - \hat{St}^2 \hat{Re}]^2 + \hat{St}^2}}, \quad (21)$$

and a phase lag  $\hat{\beta}$  behind the forcing  $[X = |X| \exp i(t' \hat{St} - \hat{\beta})]$ :

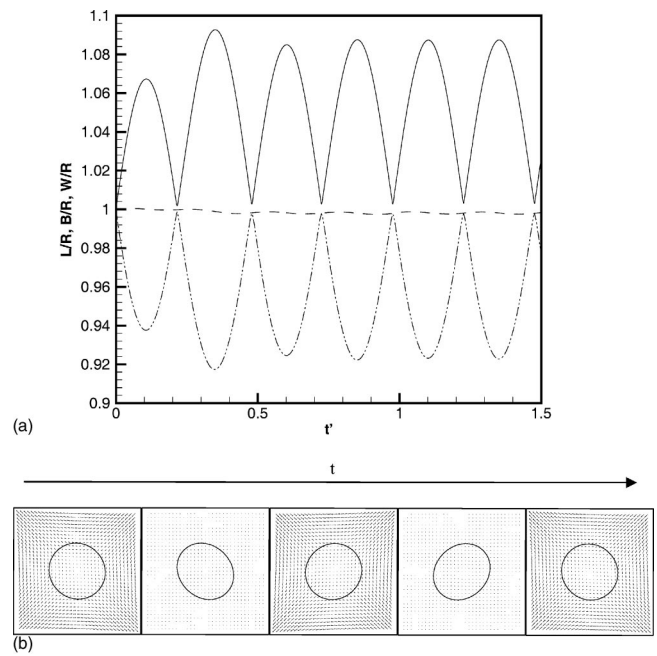


FIG. 3. (a) Drop axes evolving with nondimensional time in an oscillatory extensional flow Length- $L$  (solid), breadth- $B$  (dash-double-dotted), width- $W$  (dashed). (b) Drop shape at equal interval during one flow period;  $Re=0.1$ ,  $St=4\pi$ ,  $k=10$ .

$$\hat{\beta} = \tan^{-1} \frac{\hat{St}}{\hat{k}} (1 - \hat{k} \hat{Re} + \hat{St}^2 \hat{Re}^2). \quad (22)$$

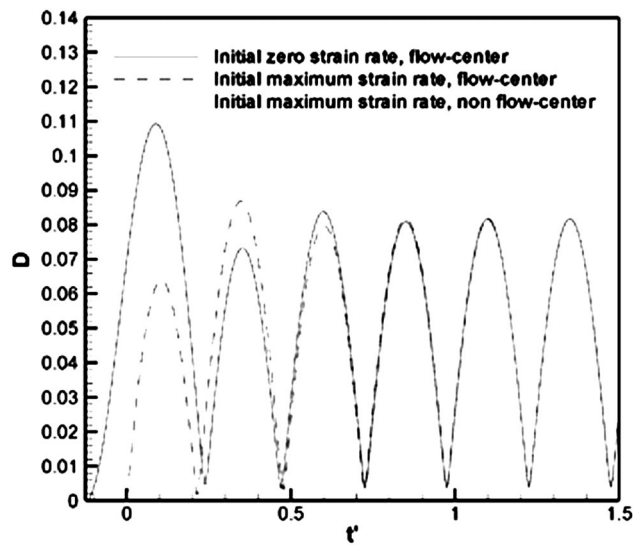
One can retrieve the Stokes limit  $|X| = \hat{k}^{-1}$  and  $\hat{\beta} = \tan^{-1}(\hat{St}/\hat{k})$ . Expression (21) indicates that resonance occurs at  $\hat{k} = \hat{St}^2 \hat{Re}$  for fixed  $\hat{St}$  and  $\hat{Re}$ , and the resonance phase  $\hat{\beta}_{res} = \tan^{-1}(\hat{St}/\hat{k})$  from Eq. (22) is the same as in the Stokes limit. Also, we note the significance of the dynamic pressure term [the last term in Eq. (18)]. In absence of this term the phase lag would become

$$\hat{\beta} = \tan^{-1} \frac{\hat{St}}{\hat{k} - \hat{Re} \hat{St}^2}. \quad (23)$$

Equations (22) and (23) obtain different behaviors and different limits as  $\hat{k} \rightarrow \infty$  or  $\hat{St} \rightarrow \infty$ . The model variable  $X$  represents the deformation or stretching of the drop as will be appropriately defined later. Note that this model is only qualitative, and may not quantitatively compare with the simulation. However, we claim that it contains the essential physics, and therefore will accurately describe the observed trends and various scalings, as will be seen below.

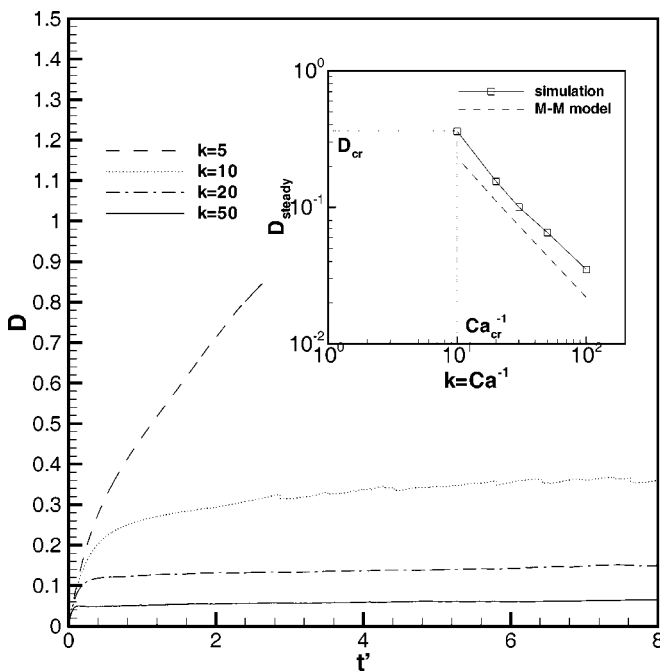
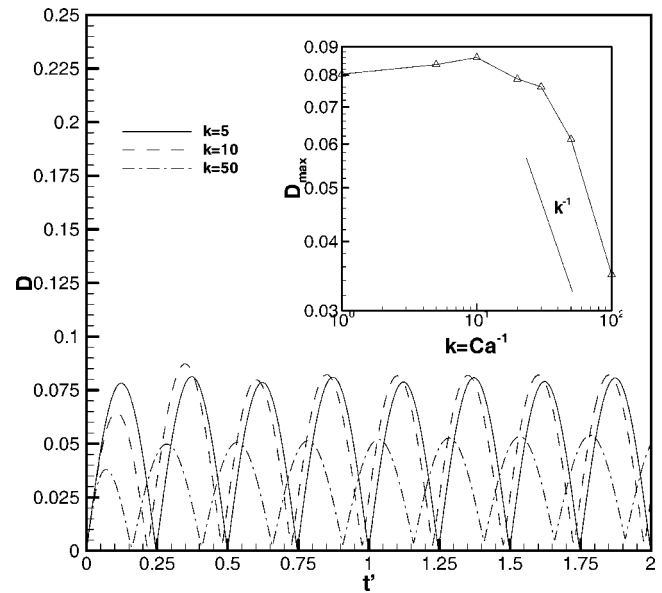
### VII. RESULTS

We simulated an isolated drop in a box-shaped domain as shown in Fig. 2. The domain is discretized by an  $81 \times 81 \times 81$  grid. An oscillating extensional flow [Eq. (1)] is imposed at the domain boundary. The radius of the undeformed drop is 0.1 of the domain size. We ensured that simulations are independent of the size of the domain. We also investigated grid convergence by increasing the discretiza-

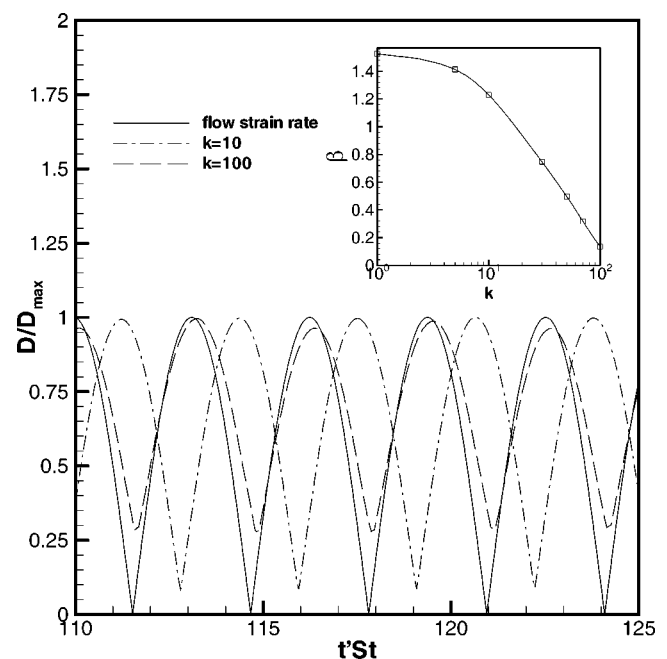
FIG. 4.  $D$  vs  $t'$  for different initial conditions;  $Re=0.1$ ,  $St=4\pi$ ,  $k=10$ .

tion to  $129 \times 129 \times 129$  without finding significant change in the result. See Sarkar and Schowalter<sup>29</sup> for detail convergence study and comparison with Stokes flow for a two-dimensional version of the algorithm.

Experimental study of the three-dimensional drop shape under shear flow<sup>39</sup> showed that the drop maintains an ellipsoidal shape up to moderate deformations. In Fig. 3(a), we plot the three drop axes with nondimensional time  $t' = t\dot{\epsilon}_0$ . The maximum  $L$  and minimum  $B$  axes are the maximum and minimum distances of the drop surface from its center within the plane of the imposed flow. The width  $W$  is in the  $z$  direction perpendicular to the plane of the flow. The drop deforms from a spherical shape  $L=B=W=R$ . After a transient period

FIG. 5.  $D$  vs  $t'$  for different  $k$  in steady extensional flow.  $St=0$ ,  $Re=0.1$ . Inset shows  $D_{steady}$  vs  $k$  along with Maffettone-Minale (MM) model.FIG. 6.  $D$  vs  $t'$  for different  $k$ ;  $St=4\pi$ ,  $Re=0.1$ . Inset shows  $D_{max}$  vs  $k$ .

each axis reaches a steady oscillating state. It is noted that  $W/R$  departs from 1.0, which indicates that a small deformation exists in the third dimension. In Fig. 3(b), top view ( $z$  direction) of the drop in the oscillating flow is shown together with the flow field in the plane through the center of the drop. The drop alternately experiences stretching in orthogonal directions. Within one period of the flow, the deformation reaches maximum twice. The maximum deformation does not coincide with the maximum strain rate (velocity) of the flow (first, third, and fifth frames), indicating a phase difference between the deformation and the strain rate.

FIG. 7.  $D/D_{max}$  vs  $t' St$  for different  $k$ . Inset shows the phase lag  $\beta$  vs  $k$ .  $St=4\pi$ ,  $Re=0.1$ .

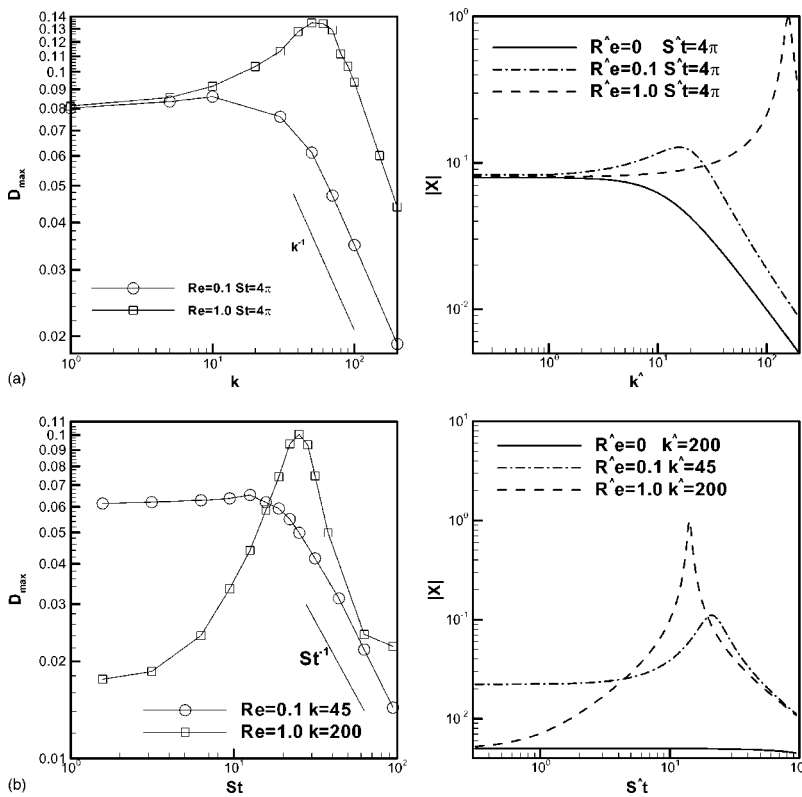


FIG. 8. (a)  $D_{\max}$  vs  $k$  and ODE predictions,  $|X|$  vs  $\hat{k}$ ; (b)  $D_{\max}$  vs  $St$  and ODE prediction,  $|X|$  vs  $\hat{St}$ .

For a nearly spherical drop, a criterion for deformation was suggested by Taylor,<sup>3,4</sup> viz.,  $D = (L - B) / (L + B)$ . In Fig. 4, we plot  $D$  as a function of nondimensional time  $t'$ . After an initial transient,  $D$  reaches a steady oscillating state where the maximum and the minimum reach their long-time values  $D_{\max}$  and  $D_{\min}$ , respectively. The nonzero  $D_{\min}$  (nonspherical shape) was also observed for drops in oscillatory shear.<sup>27,25</sup> The presence of viscosity gives rise to a finite relaxation time preventing recovery of the spherical shape. As shown in Fig. 3(b), within one period of the flow, the drop experiences the same stretching in two orthogonal directions. As a result, the oscillating frequency of  $D$  is twice the flow frequency. In Fig. 4, we compare the evolution of  $D$  under different initial strain rates. The spherical drop is introduced in the flow at the instant of minimum (zero) and maximum strain rates, respectively. For initial zero strain rate (solid line),  $D$  first shoots to a higher maximum value. As the flow reverses,  $D$  then decreases to a minimum. Thereafter lower maxima appear; maxima and minima asymptotically approach  $D_{\max}$  and  $D_{\min}$ . For an initial strain rate at its maximum (dashed and dotted lines),  $D$  does not overshoot in the first period. Although the drop experiences different startup transients for different initial conditions, eventually identical long-time evolutions are achieved. In the same plot, the history of  $D$  for a drop initially at the flow center (dashed line) and another initially away from the flow center (dotted line) are compared. Indistinguishable evolution of  $D$  is observed for these two cases. The drop is subjected to the same strain rate  $\dot{\epsilon} = \dot{\epsilon}_0 \cos(\omega t)$  independent of its position in the linear flow [see Eq. (1)] leading to identical deformation. In the following, we look at the influences of interfacial tension, flow frequency, and Reynolds number on the drop dynamics.

### A. Drop deformation: Steady extension and effects of oscillation

We first investigate the drop deformation in a steady extensional flow in Fig. 5 as a benchmark. We consider a relatively low Reynolds number of  $Re = 0.1$ . The evolution of  $D$  is plotted for different interfacial tension parameter  $k$ . At low values of  $k$  ( $k = 5.0$ ), the drop experiences continuous stretching without reaching an equilibrium indicating eventual breakup. As  $k$  is increased to 10.0, the extensional growth is restrained by increased interfacial tension.  $D$  reaches a steady value after a transient evolution. We found that above  $k = 10.0$  a steady deformation  $D_{\text{steady}}$  exists in the long-time limit, while below  $k = 10.0$  the drop breaks up after transients. Such a critical  $k_{cr}$  (or a critical capillary number  $Ca_{cr} = k_{cr}^{-1}$ ) has been experimentally observed and predicted by various analytical models. In the inset, the variation of  $D_{\text{steady}}$  with  $k$  is plotted. The Maffettone–Minale (MM) model<sup>17</sup> (dash-dotted line) slightly underpredicts the numerical simulation. The predicted critical deformation  $D_{cr} \approx 0.35$  and the corresponding critical capillary number  $Ca_{cr} \approx 0.1$  agree with the experimental results in the Stokes flow limit.<sup>14</sup> The observed  $k^{-1}$  scaling agrees with the prediction of small-deformation theory ( $D \sim Ca$ ).

We turn to drop deformation in an oscillating extensional flow. In Fig. 6 the evolution of  $D$  for different  $k$  is plotted to demonstrate the effects of interfacial tension. In contrast to steady extension (Fig. 5), a bounded shape is achieved even at  $k = 5.0$ , and for  $k = 10.0$  a lower deformation is observed. Oscillating extensional flow prevents drop breakup even at very small interfacial tensions because the flow reverses before the drop could break. In the inset, the variation of  $D_{\max}$

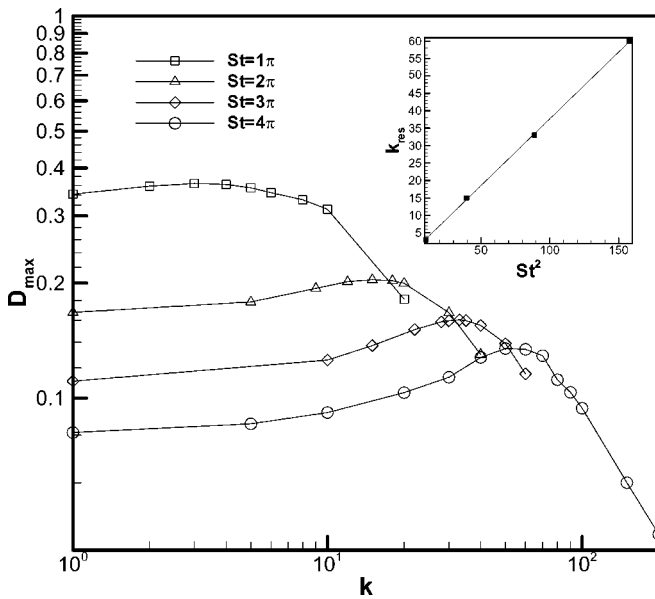


FIG. 9.  $D_{\max}$  vs  $k$  for different  $St$ ;  $Re=1.0$ . Inset shows the scaling of  $k_{res} \sim St^2$ .

with  $k$  is plotted. For values of  $k < 10$ ,  $D_{\max}$  shows a slight increase with increasing  $k$ ; as in the two-dimensional case<sup>29</sup> it represents a resonance phenomenon characteristic of a finite inertia system. The system behaves like a harmonic oscillator, having a natural frequency varying with the interfacial tension  $k$ . If the natural frequency and forcing frequency match, the drop experiences an enhanced deformation. In the inset of Fig. 6,  $D_{\max}$  is seen to scale as  $k^{-1}$  for  $k \rightarrow \infty$ . A similar linear relation between  $D_{\max}$  and the strain rate am-

plitude in the small-deformation range was also reported in the previous oscillatory-shear study.<sup>25</sup> Below we will use the ODE model of Sec. VI to qualitatively explain the drop response including various asymptotes with  $|X|$  acting as a surrogate for  $D_{\max}$ .

For the same flow, different  $k$  leads to different phases for  $D$  as is seen in Fig. 6. In Fig. 7, we plot the scaled deformation  $D/D_{\max}$  vs the scaled time  $t' St$  after the initial transient. For comparison, the absolute strain rate  $|\dot{\epsilon}/\dot{\epsilon}_0| = |\cos(\omega t)|$  (solid line) is also shown in the same figure. The deformation lags behind the strain rate. In the inset of Fig. 7, the phase lag  $\beta$  of the deformation behind the flow strain rate is plotted as a function of  $k$ . It shows that the deformation lags by a value between 0 and  $\pi/2$ . At low interfacial tension ( $k \rightarrow 0$ ),  $\beta$  approaches  $\pi/2$ . With increasing  $k$ ,  $\beta$  decreases. Both are predicted by the ODE model (22) for low  $Re$ , as is the case here.

We conclude that the introduction of oscillation in an imposed extensional flow leads to an oscillating drop shape, which tends to settle down in the long-time limit to a periodic behavior with a phase lag behind imposed strain rate. As in the two-dimensional case<sup>29,30</sup> finite inertia results in a resonance of the system. In the following, we explore these phenomena in detail, and explain the observation with the ODE model.

**B. Deformation: Resonance and phase dynamics**

We increase the Reynolds number to 1.0. In Fig. 8(a), the variation of deformation  $D_{\max}$  with interfacial tension  $k$  is shown for both  $Re=0.1$  and  $Re=1.0$  at  $St=4\pi$ . As  $k$  increases,  $D_{\max}$  first increases to a peak, and then decreases.

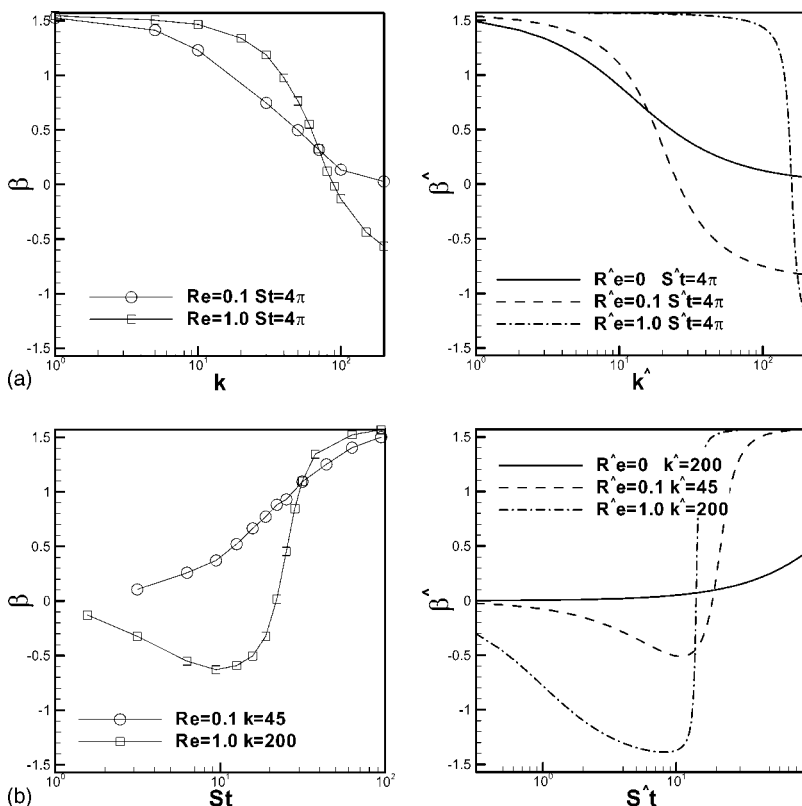


FIG. 10. (a)  $\beta$  vs  $k$  and ODE predictions,  $\hat{\beta}$  vs  $\hat{k}$ ; (b)  $\beta$  vs  $St$  and ODE prediction  $\hat{\beta}$  vs  $\hat{St}$ .

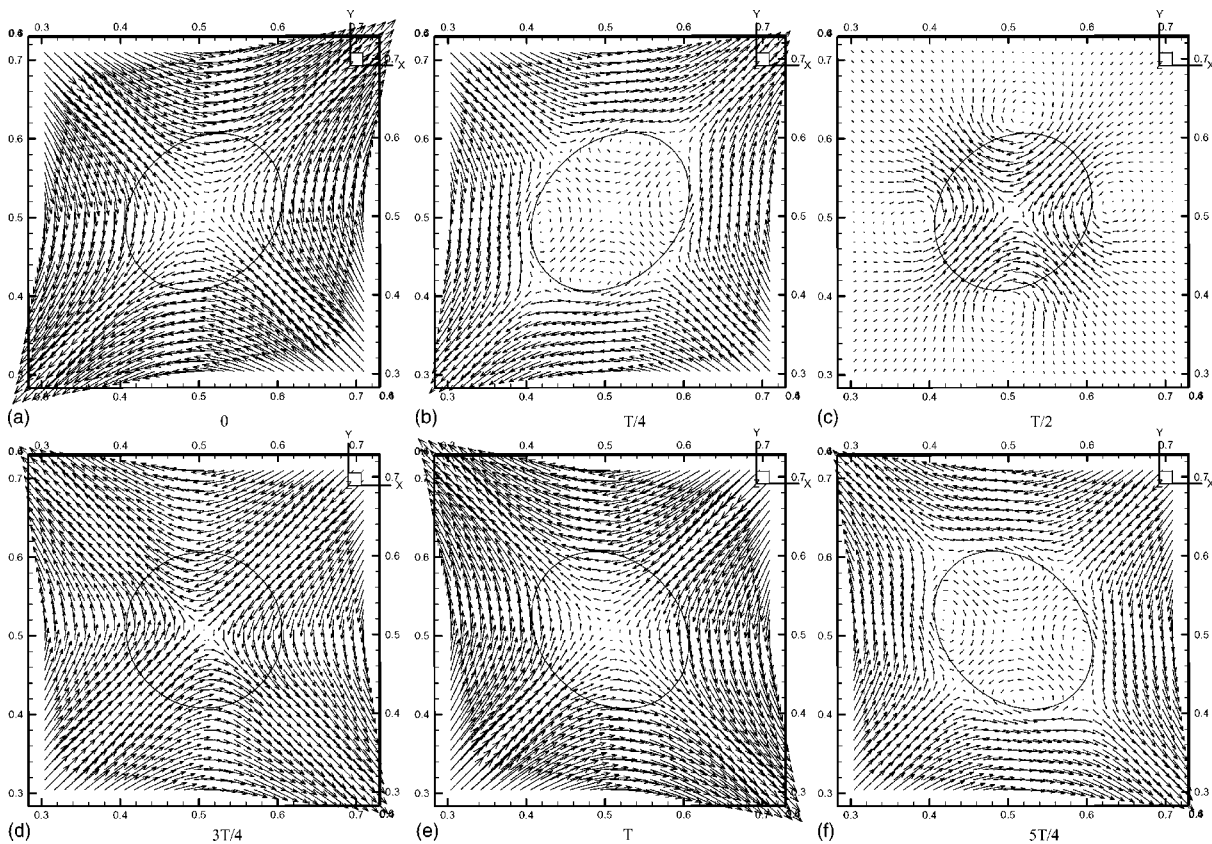


FIG. 11. Drop-flow interaction at steady oscillating state for different time instants;  $St=4\pi$ ,  $k=50$ ,  $Re=1.0$ .

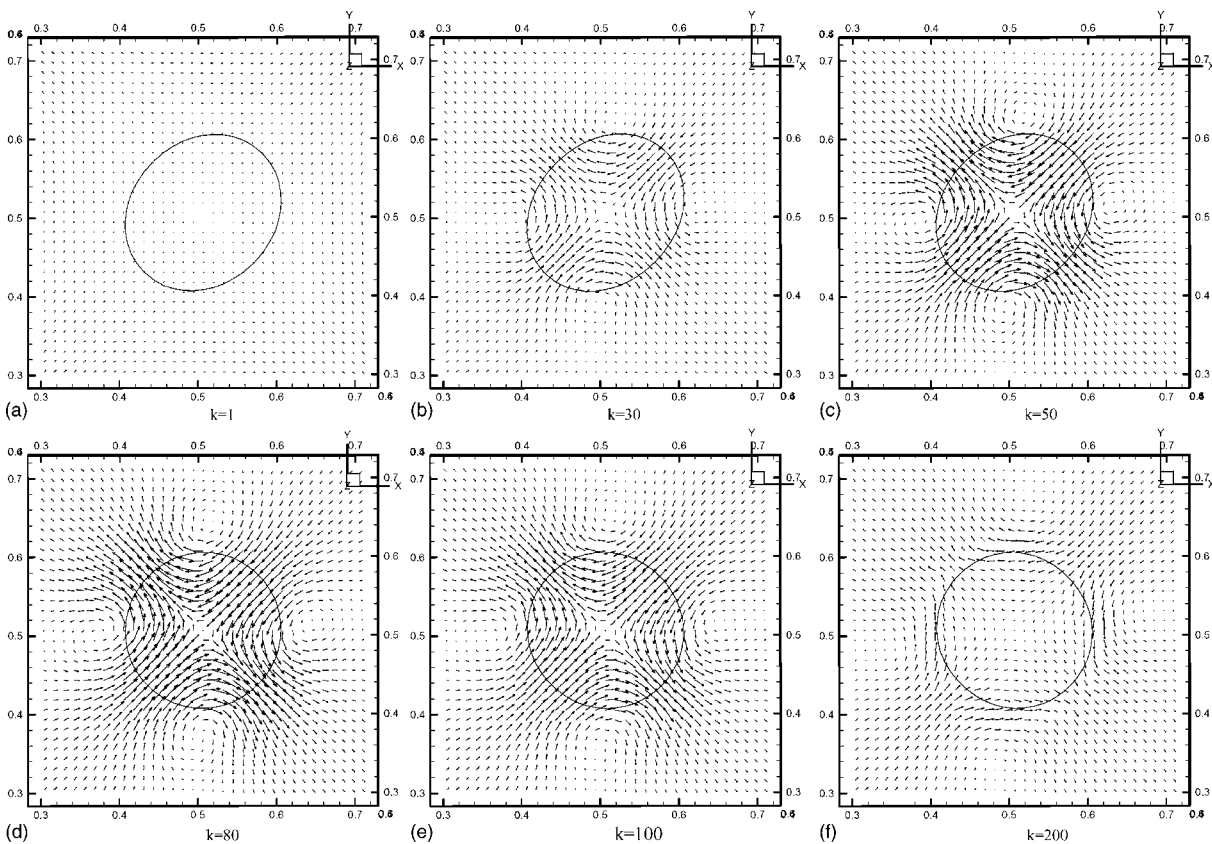


FIG. 12. Flow perturbation due to drop at different  $k$ ;  $St=4\pi$ ,  $Re=1.0$ .

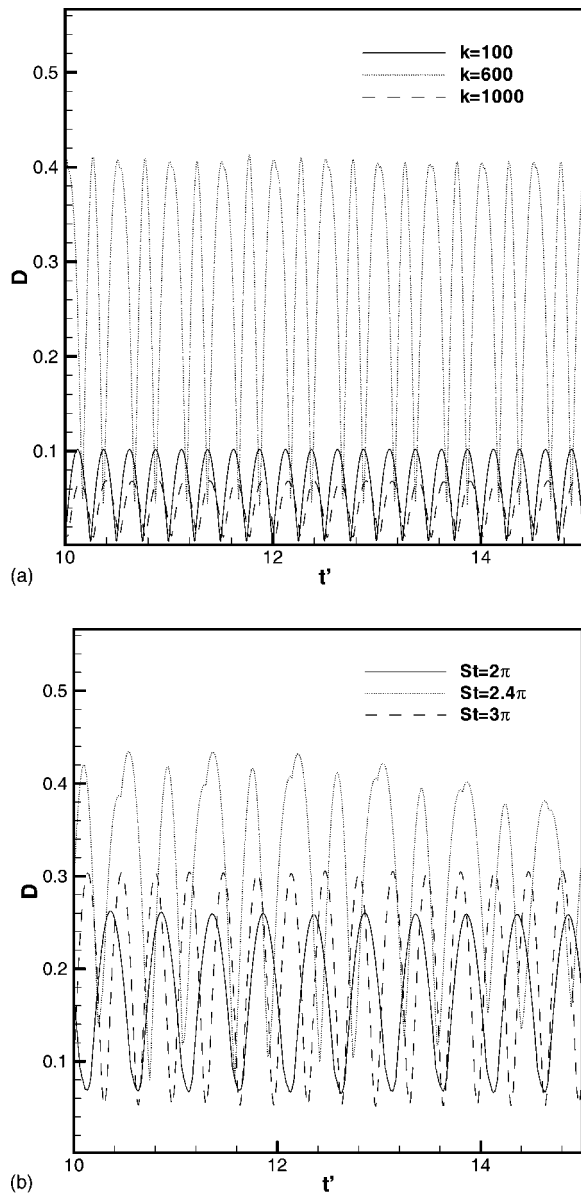


FIG. 13. (a)  $D$  vs  $t'$  for different interfacial tensions at  $St=4\pi$ ,  $Re=10.0$ . (b)  $D$  vs  $t'$  for different frequencies at  $k=200$ ,  $Re=10.0$ .

Increased inertia leads to a more prominent resonance peak  $D_{\max} \approx 0.138$  for  $Re=1.0$  compared to  $D_{\max} \approx 0.09$  at  $Re=0.1$ . In Fig. 8(b), we show variation of  $D_{\max}$  with nondimensional frequency  $St$  at fixed  $k$  for  $Re=0.1$  and  $Re=1.0$ . As with  $k$ ,  $D_{\max}$  increases to a resonant peak (more distinct in the case of  $Re=1.0$ ) before decreasing with increasing  $St$ . The system has a natural frequency determined by the interfacial tension (fixed  $k$ ). When the forcing frequency  $St$  matches the natural frequency, the system shows enhanced resonant response. For larger  $St$ , the increased forcing frequency leads to a decreased drop deformation, with  $D_{\max}$  varying as  $St^{-1}$ . At high frequency, the magnitude of flow strain  $|\varepsilon|$  is small due to the frequent flow reversal ( $|\varepsilon| = 1/St$ ). The deformation  $D_{\max}$  is small for such small strains.

We resort to the ODE model to explain the observed drop dynamics. In Figs. 8(a) and 8(b), we also plot  $|X|$  [Eq. (21)] as functions of both  $\hat{k}$  and  $\hat{St}$  for  $\hat{Re}=0, 0.1$ , and  $1.0$ .

For Stokes flow ( $\hat{Re}=0$ ), we observe no resonance with  $|X|$  decreasing monotonically with increasing  $\hat{k}$  or  $\hat{St}$ . As  $\hat{Re}$  is increased to  $0.1$  (dash-dotted lines) and  $1.0$  (dashed lines),  $|X|$  shows resonance behavior with increasing  $\hat{k}$  or  $\hat{St}$ , similar to the simulation results. The resonance peak increases with increased  $\hat{Re}$ . The model also predicts  $\hat{k}^{-1}$  and  $\hat{St}^{-1}$  scaling for  $|X|$  similar to  $D_{\max}$ . Note that in the absence of the last term in Eq. (18) due to dynamic pressure, the model would have wrongly predicted a  $\hat{St}^{-2}$  scaling. Recall that the model can only predict various qualitative trends, and cannot be trusted for quantitative comparison with simulations. It can perhaps be carefully calibrated to match the actual simulations. However, here we have not undertaken such a task.

In Fig. 9, we have plotted  $D_{\max}$  as a function of  $k$ , for different forcing frequencies  $St$ , for  $Re=1.0$ . The resonant peak occurs for larger  $k$  with larger  $St$ , indicating that the natural frequency increases with the spring element, i.e., the interfacial tension. In the inset, we see that the value of  $k$  at resonance  $k_{res}$  is a linear function of  $St^2$ . Indeed, from the ODE [Eq. (21)], we see that resonance takes place for  $\hat{k}_{res} \sim \hat{St}^2 \hat{Re}$ . Also the ODE predicts that the resonant value of deformation variable  $|X|$  decreases with  $\hat{St}$  as seen in the simulation.

In Fig. 10, we plot the phase lag  $\beta$  for the same cases as in Fig. 8, along with its ODE analog  $\hat{\beta}$ .  $\beta$  decreases with increasing  $k$  [Fig. 10(a)]. In contrast to  $Re=0.1$ ,  $\beta$  becomes negative for  $k > 90$ , at  $Re=1.0$ , which represents a *phase ahead of the strain rate*. Also for the higher Reynolds number case,  $\beta$  asymptotically approaches a nonzero value  $\beta_{k \rightarrow \infty} \approx -0.5$ . The model expression displays qualitatively similar trends, as we progressively increase model Reynolds number  $\hat{Re}$  from the Stokes flow. For Stokes flow, the phase [ $\hat{\beta} = \tan^{-1}(\hat{St}/\hat{k})$ ] is restricted to the range  $[0, \pi/2]$ . The  $Re=0.1$  simulation matches better with the model Stokes flow than with the  $\hat{Re}=0.1$  model result. As mentioned before, such discrepancy is expected from the qualitative model. The negative  $\beta$  value at increased value of  $Re$  can be explained by noting that the negative second term in Eq. (22) eventually dominates the other two terms. The curves of  $\hat{\beta}$  (as function of  $\hat{k}$ ) for nonzero  $\hat{Re}$ , cross that for  $\hat{Re}=0$  at a value  $\hat{k} = \hat{St}^2 \hat{Re}$  corresponding to resonance. As has been shown in Sec. IV,  $\hat{\beta}_{res}$  at resonance for nonzero  $\hat{Re}$  is the same as  $\hat{\beta}$  for  $\hat{Re}=0$ . Figure 10(b) shows  $\beta$  as a function of  $St$  at constant  $k$  for  $Re=0.1$  and  $Re=1.0$ . For steady extension ( $St=0$ )  $\beta=0$  as expected. For  $Re=0.1$ ,  $\beta$  increases with the increase of flow frequency  $St$ . However, for the higher inertia case ( $Re=1.0$ ),  $\beta$  first decreases to attain a negative minimum, and then increases to become positive. The model prediction is qualitatively similar (model Stokes flow is similar to the  $Re=0.1$  simulation). At relatively large  $\hat{k}$  ( $\hat{k} > 1/\hat{Re}$ ), with increasing  $\hat{St}$   $\hat{\beta}$  becomes negative [see Eq. (22)], reaches a minimum, and then increases to positive values. The phase and its analog finally approach  $\pi/2$  behind the strain rate  $\dot{\varepsilon}$  but in phase with the flow strain  $\varepsilon$ , as  $St \rightarrow \infty$ . Here also we note the significance of the dynamic pressure term. The

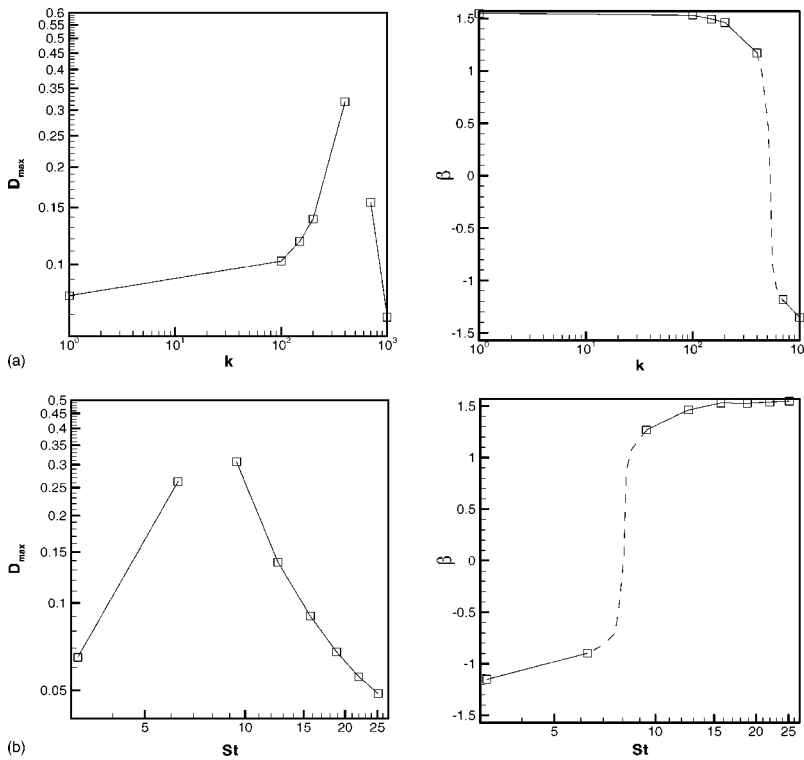


FIG. 14. (a)  $D_{max}$  and  $\beta$  vs  $k$  at  $St=4\pi$ ,  $Re=10.0$ . (b)  $D_{max}$  and  $\beta$  vs  $St$  at  $k=200$ ,  $Re=10.0$ .

model  $\hat{\beta}$  without it [Eq. (23)] would be very different; it approaches zero as  $\hat{St} \rightarrow \infty$ .

### C. Effects of deformation on flow field

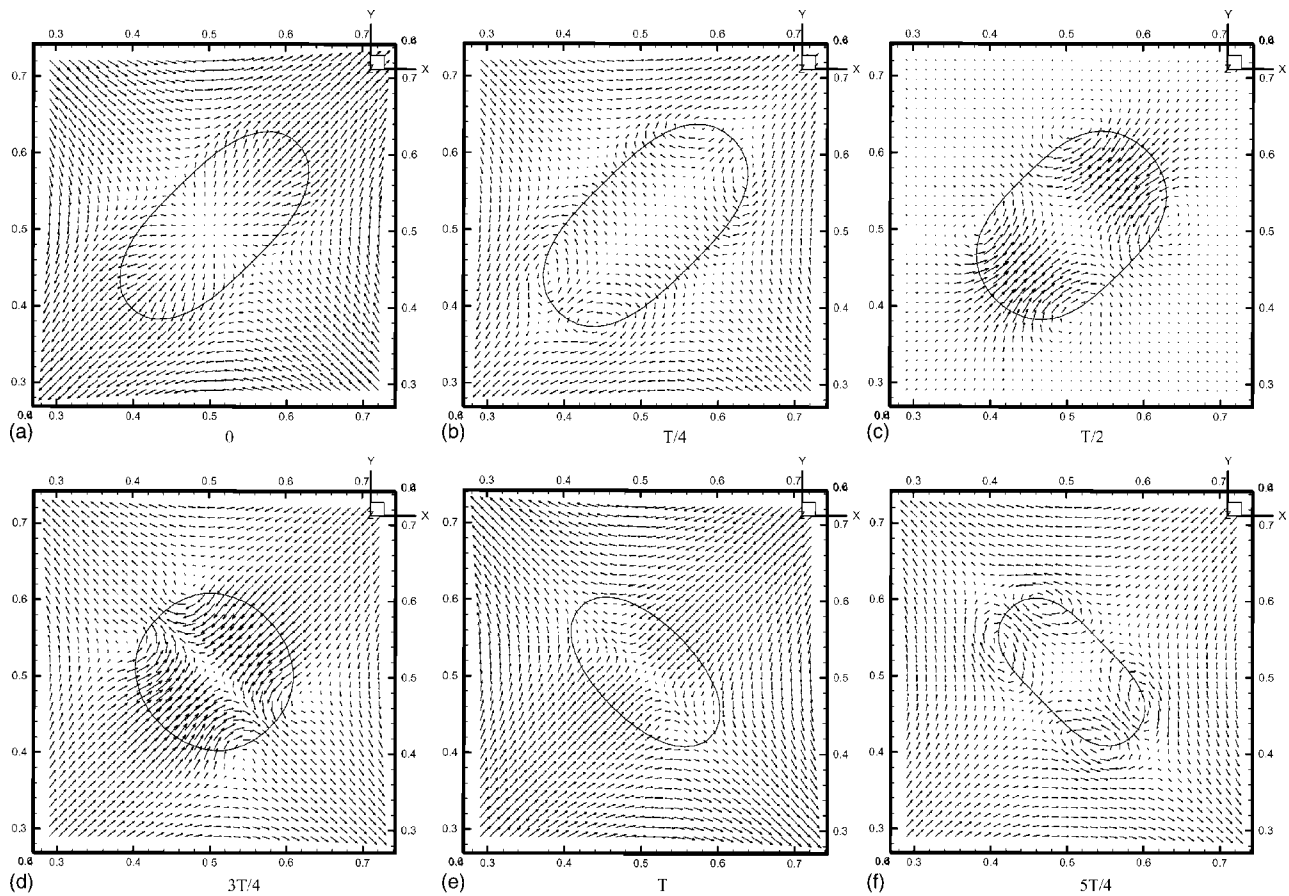
While the drop deforms in response to the imposed extensional flow, presence of the drop significantly changes the flow itself. Note that for the density and viscosity matched cases considered here, the drop is felt due to the nonzero value of interfacial tension. In Fig. 11, we examine the structure of the flow around and inside the drop. The snapshots are taken at different time instants [ $T$  represents half period of the imposed flow; in this time the drop reaches from one maximum in Fig. 11(b) to another in Fig. 11(f) in an orthogonal direction]. Viewed from the top ( $z$  direction), the drop is stretched in two orthogonal directions in the plane of the flow. At  $T/4$  with strain rate  $\dot{\epsilon}$  reducing, four vortices and nine stagnation points appear inside the drop. At  $T/2$ , the velocity of the imposed flow is zero while the figure demonstrates the perturbed flow due to the presence of the drop. The vortices are stronger than those at  $T/4$ . The centers of the vortices appear outside the drop. At  $3T/4$ , the perturbed flow and the deformation are different from those at  $T/4$ , although the imposed flow is identical except for the axes of extension being orthogonal. In contrast to  $T/4$ , the drop deforms much less with no prominent vortex structure. This indicates an asymmetry in the extending and contracting parts of a cycle of drop dynamics as well as a phase lag already seen between the drop deformation and the flow field.

In Fig. 12, we compare the perturbed flow at  $T/2$  (it corresponds to the zero velocity of the imposed oscillating flow) for different interfacial tension parameter  $k$ . Similar to

$D_{max}$ , the strength of the perturbed flow first increases, and then decreases with increased interfacial tension. Except for very small  $k=1$ , there appear four vortices at the interface. The vortices gradually move away from the drop center as  $k$  increases. The vortex structure indicates significant vorticity generation. Note that the imposed oscillating extensional flow is free of vorticity. Finite interfacial tension leads to vorticity generation at the interface. The strength of generation is dependent on both the value of interfacial tension and deformation. At high interfacial tension, the drop does not deform significantly resulting in smaller vorticity [see Fig. 12(f) for  $k=200$ ].

### D. Resonant drop dynamics and flow field at higher inertia

With the inertia of a system increased, one would expect more energetic dynamics especially at resonance. In Fig. 13, we investigate variation of  $D$  with interfacial tensions and flow frequencies at  $Re=10.0$ .  $D$  for various  $k$  at fixed  $St=4\pi$  in Fig. 13(a) attains highest value for  $k=600$  indicating a match of the natural and forcing frequency. Figure 13(b) investigates the effects of varying  $St$  at a fixed  $k=200$ . The resonance occurs at  $St=2.4\pi$ . We observe that unlike lower  $Re$ , at resonance ( $St=2.4\pi$ ), the time evolution of  $D$  does not seem to settle down to a steady periodic motion, and therefore does not result in a single value for long-time  $D_{max}$ . In Fig. 14, we plot the long-time  $D_{max}$  and phase lag  $\beta$  with  $k$  and  $St$ . Due to the difficulty in determination,  $D_{max}$  near resonance is not plotted. Note also that unlike the cases with lower  $Re$ , here deformation is much larger at resonance. For example,  $D=0.5$  corresponds to  $L/B \approx 3$ . At  $Re=10.0$ , in agreement with the ODE model, the resonance shifts towards

FIG. 15. Drop-flow interaction at  $St=2.4\pi$ ,  $k=200$ ,  $Re=10.0$ .

higher interfacial tension ( $k_{res} \approx 600$ ) and lower frequency ( $St_{res} \approx 2.4\pi$ ) compared to  $Re=1.0$  ( $k_{res} \approx 50$  and  $St_{res} \approx 8\pi$ ) and follows the scaling  $\hat{k}_{res} \sim \hat{St}^2 \hat{Re}$ .  $\beta$  varies sharply near resonance as well; the continuously evolving dynamics precludes precise values in this region (see also Fig. 10).

We concentrate on the drop dynamics near resonance. Top view of the drop along with the flow field in the plane passing through the drop center is plotted in Fig. 15 for a case close to resonance ( $k=200$ ,  $St=2.4\pi$ ). As mentioned above, the deformation continues to evolve without settling down to a periodic motion. We consider a half-period  $T$  of the flow starting at  $t'=15\pi/4$ . The length of velocity vectors is decreased compared to Fig. 11 for clarity of presentation. In contrast to  $Re=1.0$  (Fig. 11), difference in drop shapes one period apart [Figs. 15(b) and 15(f)] indicates the nonperiodic motion. Figure 15(b) shows four strong vortices appearing at the interface. The vortices further elongate the drop in one direction and squeeze the drop in the orthogonal direction, resulting in a narrow waist at  $T/4$ . At  $T/2$ , with zero imposed strain rate, the perturbed flow is directed in the opposite direction, squeezing at the head and extending at the waist, resulting in a barrel-like shape. The appearance of the barrel-like shape has been reported by Ramaswamy and Leal *et al.*<sup>20</sup> for bubbles in a pure extensional flow. In Fig. 16 we plot three-dimensional drop shapes (for the same time instants as in Fig. 15) in top and side views. We observe the lack of periodicity in the drop dynamics as well as significant

deformation in the  $z$  direction for this case. Indeed, squeezing in the  $x$ - $y$  plane leads to extension in the orthogonal direction to ensure incompressibility. The large deformation of drop leads to significant modification of the surrounding flow field (see Fig. 15). We investigate the strong nonlinear aperiodic behavior at resonance by examining the frequency response of the drop. In Fig. 17(a) fast Fourier transform (FFT) of  $D(t)$  displays a strong subharmonic component that is 20 times in magnitude compared to the fundamental component. In one flow period, the drop shape, while executing periodic dynamics, undergoes two periods in two orthogonal directions [Fig. 3(b)]. Therefore, at the current flow frequency  $St=\omega/\dot{\gamma}=2.4\pi$ , the nondimensional forcing frequency for the drop deformation  $D$  is  $2St=4.8\pi$ . In Fig. 17(a) the strong peak at  $2.4\pi$  corresponds to the subharmonic, and the small one at  $4.8\pi$  is the fundamental. Away from resonance, the periodically evolving  $D$  at  $St=2\pi$  and  $k=200$  [Fig. 13(b)] shows only a fundamental component at  $4\pi$  in the frequency spectrum [Fig. 17(b)]. Often in nonlinear system, appearance of subharmonic indicates the onset of transition to completely chaotic motion.<sup>40</sup> We note that the present problem with a deforming drop is nonlinear even without inertia due to the fact that the boundary condition is prescribed at a moving interface which is determined as a part of the solution. Such nonlinearity in Stokes flow results in multiple states of deformable drops.<sup>41</sup> However, for the lower Reynolds number cases, the drop dynamics did not

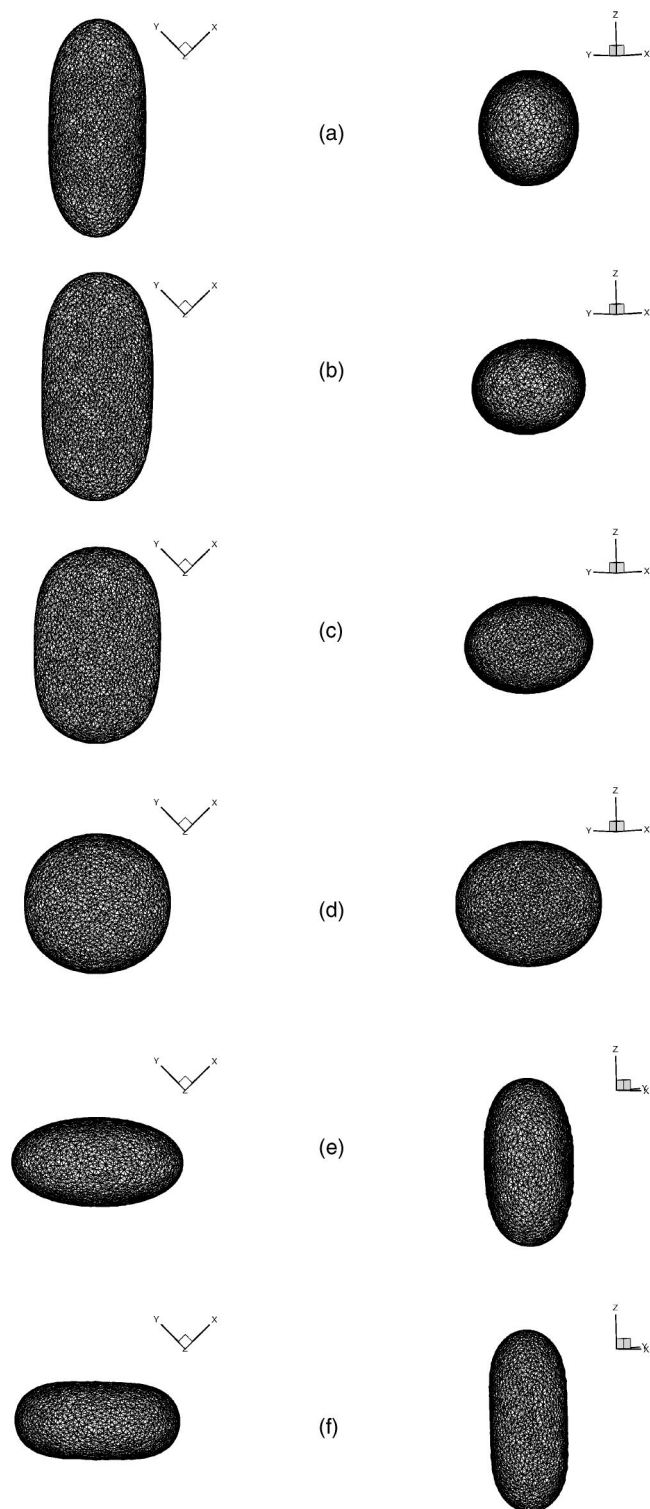


FIG. 16. Drop shapes (top and side views) at same time instants as Fig. 15,  $St=2.4\pi$ ,  $k=200$ ,  $Re=10.0$ .

display such aperiodic behaviors for the parameters considered. With the inclusion of inertia, the convective term in Eq. (2) contributes to additional nonlinearity, which at resonance leads to observed subharmonic response.

### VIII. CONCLUSION

We have used direct numerical simulation (DNS) to investigate drop deformation in an oscillating extensional flow at nonzero Reynolds number. Such a flow can be realized in

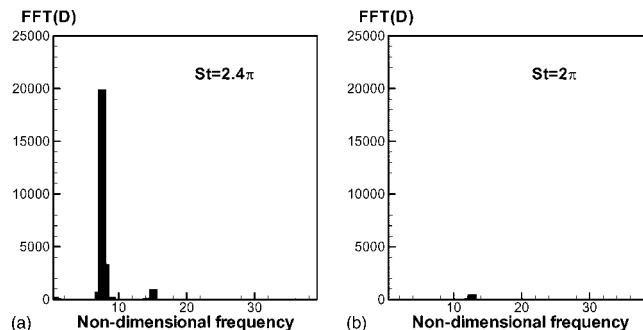


FIG. 17. FFT of  $D$  (a) at resonance  $St=2.4\pi$ ,  $k=200$  and (b) at nonresonance  $St=2\pi$ ,  $k=200$ .

a four-roll mill. It can profitably be used to examine time-dependent nonviscometric rheology of emulsions and polymeric blends. In this flow the drop undergoes an oscillating deformation that settles down after initial transient to a periodic motion with a phase lag as well as a maximum and a minimum deformation. Inertia plays an important role in the deformation and the surrounding velocity field. As expected, nominal oscillation tends to decrease the maximum deformation compared to steady extension. However, presence of inertia leads to a case of resonance characterized by increased deformation as was previously seen in a two-dimensional investigation.<sup>29,30</sup> The drop at finite Reynolds number represents a damped mass-spring system having a characteristic natural frequency; the interfacial tension and the viscosity act as spring and damping elements. The imposed flow field represents a periodic forcing. The deformation reaches a maximum when the forcing frequency matches the natural frequency. Along with the magnitude of deformation, in this paper we also performed a detailed investigation of its phase. The phase displays both positive and negative values and complex nonmonotonic variations with interfacial tension, inertia, and frequency.

A simple ODE model is developed that captures the essential physics of deformation, and successfully explains the observed changes in the sign of phase and asymptotic scaling at large values of interfacial tension and frequency. At finite inertia, a dynamic pressure arises due to the periodic flow, which plays a critical role in determining the deformation. It leads to an extra forcing term in the ODE apart from the viscous forcing due to the imposed flow. The dynamic pressure is responsible for negative phase of deformation at higher inertia. A negative deformation phase has profound implications in the effective stresses in such emulsions. Note that in an oscillatory-shear rheometry, a fluid is subjected to a given oscillatory strain field; the in-phase and the out-of-phase parts of the resulting stress determine the elasticity and the viscosity of the fluid. Similar tests can be performed at finite Reynolds number to obtain inertial rheology, which will be of critical importance in many industrial emulsion flows, and will be investigated in future work.

As the imposed flow deforms the drop, the drop modifies the flow. Although the imposed extensional flow is free of vorticity, the presence of interfacial tension (we consider only density and viscosity matched cases) leads to vorticity

generation. Vorticity generation is an important mechanism for modifying the vortex structure of a turbulent flow with possible applications in drag reduction. With increased deformation at higher Reynolds number such effect on the flow also increases. For larger Reynolds number, at resonance the drop deformation becomes highly nonlinear, and fails to reach a periodic motion. It is also marked by the appearance of strong subharmonic component that indicates a possible route to chaotic motion upon further increase of inertia. The inertia-induced resonance offers an alternative mechanism for drop breakup at relatively lower strain rate, but appropriate frequency. It is particularly relevant in turbulent flows with a wide range of length and frequency scales.

## ACKNOWLEDGMENTS

Financial support from Department of Mechanical Engineering, University of Delaware and University of Delaware Research Foundation is acknowledged.

- <sup>1</sup>C. L. Tucker III and P. Moldenaers, "Microstructural evolution in polymer blends," *Annu. Rev. Fluid Mech.* **34**, 177 (2002).
- <sup>2</sup>G. K. Batchelor, "The stress system in a suspension of force-free particles," *J. Fluid Mech.* **41**, 545 (1970).
- <sup>3</sup>G. I. Taylor, "The viscosity of a liquid containing small drops of another liquid," *Proc. R. Soc. London, Ser. A* **138**, 41 (1932).
- <sup>4</sup>G. I. Taylor, "The formation of emulsions in definable fields of flow," *Proc. R. Soc. London, Ser. A* **146**, 501 (1934).
- <sup>5</sup>R. G. Cox, "The deformation of a drop in general time-dependent fluid flow," *J. Fluid Mech.* **37**, 601 (1969).
- <sup>6</sup>C. E. Chaffey and H. Brenner, "A second order theory for shear deformation of drops," *J. Colloid Interface Sci.* **24**, 258 (1967).
- <sup>7</sup>A. Acrivos and T. S. Lo, "Deformation and breakup of a single slender drop in an extensional flow," *J. Fluid Mech.* **86**, 641 (1978).
- <sup>8</sup>E. J. Hinch and A. Acrivos, "Long slender drops in a simple shear flow," *J. Fluid Mech.* **98**, 305 (1980).
- <sup>9</sup>D. V. Khakhar and J. M. Ottino, "Deformation and breakup of slender drop in linear flows," *J. Fluid Mech.* **166**, 265 (1986).
- <sup>10</sup>M. R. Kennedy, C. Pozrikidis, and R. Skalak, "Motion and deformation of liquid drops and the rheology of dilute emulsions in simple shear flow," *Comput. Fluids* **23**, 251 (1994).
- <sup>11</sup>M. Loewenberg and E. J. Hinch, "Numerical simulation of a concentrated emulsion in shear flow," *J. Fluid Mech.* **321**, 395 (1996).
- <sup>12</sup>A. Z. Zinchenko and R. H. Davis, "Shear flow of highly concentrated emulsions of deformable drops by numerical simulations," *J. Fluid Mech.* **455**, 21 (2002).
- <sup>13</sup>H. P. Grace, "Dispersion phenomena in high viscosity immiscible fluid systems and application of static mixers as dispersion devices in such systems," *Chem. Eng. Commun.* **14**, 225 (1982).
- <sup>14</sup>B. J. Bentley and L. G. Leal, "An experimental investigation of drop deformation and breakup in steady, two-dimensional linear flows," *J. Fluid Mech.* **167**, 241 (1986).
- <sup>15</sup>S. Guido, M. Minale, and P. L. Maffettone, "Drop shape dynamics under shear-flow reversal," *J. Rheol.* **44**, 1385 (2000).
- <sup>16</sup>A. S. Almusallam, R. G. Larson, and M. J. Solomon, "A constitutive model for the prediction of ellipsoidal droplet shapes and stresses in immiscible blends," *J. Rheol.* **44**, 1055 (2000).
- <sup>17</sup>P. L. Maffettone and M. Minale, "Equations of change for ellipsoidal drops in viscous flow," *J. Non-Newtonian Fluid Mech.* **78**, 227 (1998).
- <sup>18</sup>M. Bousmina, "Rheology of polymer blends: linear model for viscoelastic emulsions," *Rheol. Acta* **38**, 73 (1999).
- <sup>19</sup>N. E. Jackson and C. L. Tucker III, "A model for large deformation of an ellipsoidal droplet with interfacial tension," *J. Rheol.* **47**, 659 (2003).
- <sup>20</sup>S. Ramaswamy and L. G. Leal, "A note on inertial effects in the deformation of Newtonian drops in uniaxial extensional flow," *Int. J. Multiphase Flow* **23**, 561 (1997).
- <sup>21</sup>I. S. Kang and L. G. Leal, "Numerical solution of axisymmetric, unsteady free-boundary problems at finite Reynolds number I. finite-difference scheme and its application to the deformation of a bubble in uniaxial straining flow," *Phys. Fluids* **30**, 1929 (1987).
- <sup>22</sup>I. S. Kang and L. G. Leal, "Numerical solution of axisymmetric, unsteady free-boundary problems at finite Reynolds number II. deformation of a bubble in biaxial straining flow," *Phys. Fluids A* **1**, 644 (1989).
- <sup>23</sup>Y. Y. Renardy and V. Cristini, "Effects of inertia on drop breakup under shear," *Phys. Fluids* **13**, 7 (2001).
- <sup>24</sup>Y. Renardy, V. Cristini, and J. Li, "Drop fragmentation distribution under shear with inertia," *Int. J. Multiphase Flow* **28**, 1125 (2002).
- <sup>25</sup>R. Cavallo, S. Guido, and M. Simeone, "Drop deformation under small-amplitude oscillatory shear flow," *Rheol. Acta* **42**, 1 (2003).
- <sup>26</sup>W. Yu and M. Bousmina, "Modeling of oscillatory shear flow of emulsions under small and large deformation fields," *J. Rheol.* **46**, 1401 (2002).
- <sup>27</sup>S. Wannaborworn, M. R. Mackley, and Y. Renardy, "Experimental observation and matching numerical simulation for the deformation and breakup of immiscible drops in oscillatory shear," *J. Rheol.* **46**, 1279 (2002).
- <sup>28</sup>J. F. Palierne, "Linear rheology of viscoelastic emulsions with interfacial tension," *Rheol. Acta* **29**, 204 (1990).
- <sup>29</sup>K. Sarkar and W. R. Schowalter, "Deformation of a two-dimensional drop at non-zero Reynolds number in time-periodic extensional flows: numerical simulation," *J. Fluid Mech.* **436**, 177 (2001).
- <sup>30</sup>K. Sarkar and W. R. Schowalter, "Deformation of a two-dimensional viscous drop in time-periodic extensional flows: analytical treatment," *J. Fluid Mech.* **436**, 207 (2001).
- <sup>31</sup>I. S. Kang and L. G. Leal, "Bubble dynamics in time-periodic straining flows," *J. Fluid Mech.* **218**, 41 (1990).
- <sup>32</sup>F. Risso and J. Fabre, "Oscillations and breakup of a bubble immersed in a turbulent field," *J. Fluid Mech.* **372**, 323 (1998).
- <sup>33</sup>H. A. Stone, "Dynamics of drop deformation and breakup in viscous fluids," *Annu. Rev. Fluid Mech.* **26**, 65 (1994).
- <sup>34</sup>H. A. Stone, B. J. Bentley, and L. G. Leal, "An experimental study of transient effects in the breakup of viscous drops," *J. Fluid Mech.* **173**, 131 (1986).
- <sup>35</sup>G. Tryggvason, B. Bunner, O. Ebrat, and W. Taubar, "Computation of multiphase flows by a finite difference front tracking method. I. Multi-fluid flows," *29th Computational Fluid Dynamics Lecture Series 1998-03* (Von Karman Institute of Fluid Dynamics, Sint-Genesius-Rode, Belgium, 1998).
- <sup>36</sup>G. Tryggvason, B. Bunner, A. Esmaeeli, D. Juric, N. Al-Rawahi, W. Taubar, J. Han, S. Nas, and Y. J. Jan, "A front-tracking method for the computations of multiphase flow," *J. Comput. Phys.* **169**, 708 (2001).
- <sup>37</sup>K. Sarkar and W. R. Schowalter, "Deformation of a two-dimensional viscoelastic drop at non-zero Reynolds number in time-periodic extensional flows," *J. Non-Newtonian Fluid Mech.* **95**, 315 (2000).
- <sup>38</sup>J. T. Davies and E. K. Rideal, *Interfacial Phenomena* (Academic, New York, 1963).
- <sup>39</sup>S. Guido and M. Villone, "Three-dimensional shape of a drop under simple shear flow," *J. Rheol.* **42**, 395 (1998).
- <sup>40</sup>L. D. Landau and E. M. Lifshitz, *Fluid Mechanics*, 2nd ed. (Pergamon, Oxford, 1987).
- <sup>41</sup>J. Blawdziewicz, V. Cristini, and M. Loewenberg, "Multiple stationary states for deformable drops in linear Stokes flow," *Phys. Fluids* **15**, L37 (2003).